Bioactive Materials 5 (2020) 387–397

Contents lists available at ScienceDirect

Bioactive Materials

journal homepage: http://www.keaipublishing.com/biomat

Mineralization of calcium phosphate controlled by biomimetic self-assembled peptide monolayers via surface electrostatic potentials

Shuo Wang[a], Yongdong Yang[b,**], Ronghan Wang[a], Xiangdong Kong[c], Xiumei Wang[a,*]

[a] State Key Laboratory of New Ceramics and Fine Processing, Key Laboratory of Advanced Materials of Ministry of Education, School of Materials Science and Engineering, Tsinghua University, Beijing, 100084, China
[b] Dongzhimen Hospital Affiliated Beijing University of Chinese Medicine, Beijing, 100700, China
[c] College of Life Sciences, Zhejiang Sci-Tech University, Hangzhou, 310018, China

ARTICLE INFO

Keywords:
Hydroxyapatite
Biomineralization
Self-assembled monolayer
Oligopeptides
Dentin phosphoprotein

ABSTRACT

The functions of acidic-rich domains in non-collagenous protein during biomineralization are thought to induce nucleation and control the growth of hydroxyapatite. The tripeptide Asp-Ser-Ser (DSS) repeats are the most common acidic-rich repeated unit in non-collagenous protein of dentin phosphoprotein, the functions of which have aroused extensive interests. In this study, biomimetic peptides $(DSS)_n$ (n = 2 or 3) were designed and fabricated into self-assembled monolayers (SAMs) on Au (111) surface as biomimetic organic templates to regulate hydroxyapatite (HAp) mineralization in 1.5 simulated body fluid (1.5 SBF) at 37 °C. The early mineralization processes and minerals deposited on the SAMs were characterized by X-ray diffraction, scanning electron microscope, and Fourier transform infrared spectroscopy analyses. The SAM-DSS9/DSS9G showed the highest capacity to induce HAp nucleation and growth, followed by SAM-DSS6/DSS6G, SAM-COOH, and SAM-OH. The SAM-$(DSS)_n$ had more negative zeta potentials than SAM-COOH surface, indicating that DSS repeats contributed to the biomineralization, which not only provided strong affinity with Ca^{2+} ions through direct electrostatic bonds, but more importantly influence surface electrostatic potentials of the assembled organic template for nucleation.

1. Introduction

Hydroxyapatite (HAp), as the main biomineral in bone and tooth tissues, has been considered as one of the most essential inorganic biomaterials for hard tissue repair [1].Unlike synthetic hydroxyapatite ceramics, nano-HAp formed via *in vivo* biomineralization process has unique hierarchical assembly with organic macromolecules, which endows the complex excellent mechanical properties and great osteogenic capacity [2,3]. Therefore, clarifying how the organic matrix mediates nano-HAp nucleation and growth should not only improve the understanding of biomineralization process in natural calcified tissues, but also give inspirations to the development of novel biomimetic materials [4]

In bone and tooth, the organic matrix that consists of a complex assemblage of collagen and non-collagenous proteins and polysaccharides performs as a polymeric framework to mediate HAp biomineralization via molecular recognition at the inorganic-organic interface including matching of charge, polarity, stereochemistry, topography, electrostatic potential etc. [5–9] It has been well recognized that collagen fibrils with a quarter-staggered periodic arrangement normally work as the insoluble structural template for HAp crystals nucleation and growth within their holes and grooves [10–12]. However, the precise role that these non-collagenous glycoproteins play in biomineralization is not sufficiently determined yet. Although the total content of the non-collagenous glycoproteins is no more than 10% among the whole organic components in bone or tooth, their functions in biomineralization are important and indispensable [13,14]. The non-collagenous glycoproteins mostly contain many acidic-rich domains, thus they are thought to expose negatively charged functional groups on the surface of the organic framework and act as nucleation inducers or growth modifiers for mineral deposition via attracting Ca^{2+} ions or Ca–P clusters [15–18]. According to classic theory of interfacial molecular recognition, the central role of the organic matrix in controlling inorganic nucleation is to lower the activation energy by reducing the

Peer review under responsibility of KeAi Communications Co., Ltd.
* Corresponding author.
** Corresponding author.
E-mail addresses: yyd8817@163.com (Y. Yang), wxm@mail.tsinghua.edu.cn (X. Wang).

https://doi.org/10.1016/j.bioactmat.2020.03.003
Received 10 February 2020; Received in revised form 5 March 2020; Accepted 6 March 2020

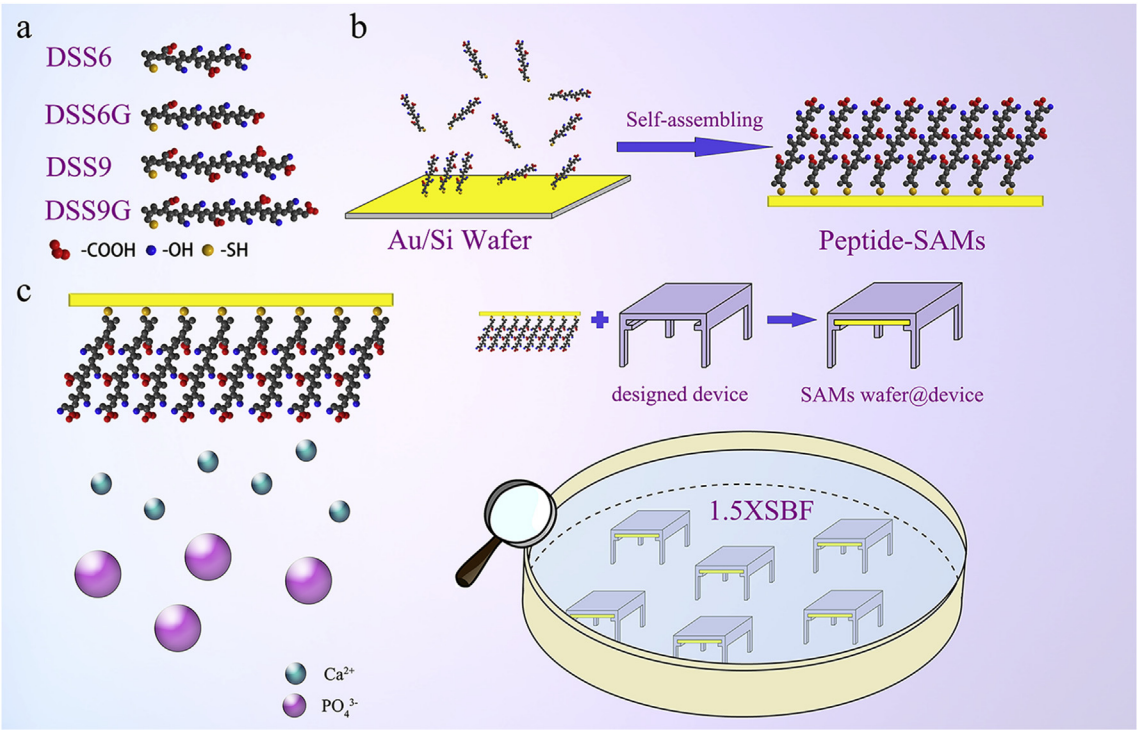

Fig. 1. (a) The molecular structures of DSS6, DSS6G, DSS9 and DSS9G peptides, the red part stands for –COOH and blue part stands for –OH; (b) The schematic diagram of an ideal SAM of DSS9 peptide supported on an Au (111) surface as an example; (c) The schematic diagram of the SAMs wafers in 1.5X SBF and the mineralization process. (For interpretation of the references to colour in this figure legend, the reader is referred to the Web version of this article.)

interfacial energy [4,8,19–21]. Therefore, we hypothesize that these polar and acidic amino acids will not only bind Ca^{2+} ions, but also change the surface electrostatic potentials to promote nucleation, even they are not fully exposed on the surface of the assembled organic framework.

Dentin sialophosphoprotein (DSPP), a kind of highly phosphorylated dentin protein, is composed of two different domains, sialylated dentin sialoprotein (DSP) and phosphorylated dentin phosphoprotein (DPP). DPP is one of the major non-collagenous proteins found in the dentin extracellular matrix and is believed to play a key role in HAp crystal formation throughout the teeth development process [22–24]. For various species of DPP, there are 35–45 residue % aspartic acid (Asp, D) and 40–55 residue % serine (Ser, S). And the tripeptide Asp-Ser-Ser (DSS) repeats (-NHCH(CH_2COOH)CONHCH(CH_2OH)CONHCH(CH_2OH)CO-) are the most repetitive unit in the amino acid sequence of DPP [13,15,18]. The functions of these repeated peptide sequences during biomineralization have aroused extensive interests. Researchers studied in *vitro* biomimetic mineralization that is regulated by analog-synthetic peptides with such sequences in attempts to uncover their roles on crystal formation [25–29]. It has been found that DPP can accelerate the nucleation and growth of HAp crystals on collagen matrix via connecting with collagen template and attracting calcium ions [13]. More than that, a variety of studies have focused on the effects of polyelectrolytic peptides. Some results showed that the negatively charged polypeptides that contain, for example, Asp or Glu had greater affinity for HAp than positively charged ones. Such substrates with more negative charge could induce more mineral deposition with greater crystal size at lower concentration [7,30,31]. Nevertheless, the functions of the negatively charged oligopeptides, especially the repeated acidic peptide domains still remain unrevealed.

In this study, the tripeptide Asp-Ser-Ser (DSS) repeats derived from DPP were chosen to construct a simple mineralization model to reveal the role of non-collagenous proteins during biomineralization. Self-assembled monolayer (SAM) is a typical and widely used mineralization template for the investigation of surface chemistry-modulated mineral crystallization. In classical SAM template models, alkanethiols that are terminated with different head groups (e.g., $–NH_2$, –OH, –COOH) could easily assemble into an overall hexagonally ordered structure of monolayer on the Au (111) substrate via the chemical bond of S and Au [30,32,33]. With this method, the SAMs with different surface chemistry were used as nucleation templates for the in *vitro* growth of calcium carbonate/calcium phosphate [34–39]. Therefore, here we designed a series of DSS repeated peptides terminated with cysteine (C) to form peptide self-assembled monolayers on Au substrates through the interactions between hydrosulphonyl (-SH) groups of cysteine residues and Au atoms. The assembled peptides that have different length of sequences (CDSSDSS (DSS6), CDSSDSSDSS (DSS9), CDSSDSSG (DSS6G), and CDSSDSSDSSG (DSS9G)) could provide uniform surfaces with similar pattern of carboxyl groups (DSS6G and DSS9G) or carboxyl/hydroxy groups (DSS6 and DSS9), serving as templates for HAp mineralization. The self-assembled biomimetic peptides monolayers SAM-$(DSS)_n$, n = 2 or 3) were immersed in simulated body fluid environment for apatite crystal nucleation and growth, comparing with other two kinds of SAMs of alkanethiols terminated with carboxyl (SAM-COOH) and hydroxyl (SAM-OH). The early mineralization processes and crystals deposited on the SAMs were characterized by X-ray diffraction, scanning electron microscope, and Fourier transform infrared spectroscopy analyses.

2. Materials and methods

2.1. Preparation of peptide SAMs on Au (111) substrate

All the oligopeptides used in this study were custom-synthesized using standard solid-phase peptide synthesis by Chinese Peptide Company (Hangzhou, China) at a purity over 89%. The sequences were listed as follows: Seq1: CDSSDSS (DSS6), Seq2: CDSSDSSDSS (DSS9), Seq3: CDSSDSSG (DSS6G), Seq4: CDSSDSSDSSG (DSS9G). Their molecular structures in space filling model were depicted in Fig. 1a.

The Au (111) substrates were prepared via coating silicon (111)

wafers with 10 nm Ti and 40 nm Au by electron beam evaporation (ANELVA L-400EK, Canon AnelvaCorporation, Kanagawa, Japan). The Au coated-silicon wafers were then cut into 10 mm × 10 mm square chips (DFD6240, DISCO, Japan), immersed in piranha solution (H_2SO_4: H_2O_2 = 7:3 v/v) for 10 min to remove organic impurities. After washing with triple-distilled water for three times, the chips were dried under nitrogen gas flow. Finally, these cleaned Au substrates were immersed in the peptide solutions (1 mg/mL) at 36.5 °C for 24 h. Once the self-assembly was finished, the specimens were rinsed with triple-distilled water to remove unattached molecules and then dried by nitrogen for further uses. Alkanethiols SAMs ($HS–(CH_2)_{11}X$, X = –COOH or –OH, Sigma, USA) were prepared with the similar procedure as control groups. These SAMs prepared in this work were abbreviated as SAM-DSS6, SAM-DSS9, SAM-DSS6G, SAM-DSS9G, SAM-COOH, and SAM-OH, respectively. The schematic diagram of the self-assembling process of the peptide was shown in Fig. 1b.

2.2. Contact angle measurement of SAMs

Water contact angles of all SAMs were measured by a contact angle meter (OCA20, Dataphysics, Germany). For each measurement, a water drop of 40 μL fell onto the surface, and the process of falling was recorded by a digital camera and analyzed via image analysis software with a resolution of 0.05°. The measurements were repeated five times at random positions on each type of SAMs surfaces.

2.3. X-ray photoelectron spectroscopy (XPS) analysis of the SAMs

XPS analysis were carried out on an X-ray photoelectron spectrometer (Escalab 250Xi, ThermoFisher, UK) using a monochromatic Al Kα X-ray source (hν = 1486.6 eV) with Carbon (284.8 eV) as a marker. The scanning area was about 300 μm × 700 μm to analyze energy state of orbital electrons in sulfur. Three spots on each kind of SAM surface were examined to give the average value.

2.4. Zeta potential measurement of the SAMs

The zeta potential of the SAM surfaces were measured by Electrokinetic Analyzer for Solid Samples(SurPASS, Anton Paar, Austria)in 0.154 M NaCl with pH adjusted to 7.4 by NaOH. The same measurements were repeated four times for each sample.

2.5. Biomimetic mineralization process in 1.5 × Simulated body fluid (SBF)

The apatite mineralization mediated by the SAMs (four oligopeptides and two alkanethiols) as well as a control sample of pure Au were carried out by immersing the chips in 1.5 SBF for up to 14 days at pH 7.4 and 37 °C, keeping the surfaces upside down in a special holder to avoid mineral deposition caused by gravity (Fig. 1c). To keep the surfaces down without touching the bottom, the holder was designed like a desk, supporting by four 'legs' with a cavity to expose the SAMs. The 1.5 SBF was a Ca–P supersaturated solution, the ionic concentrations of which were: 3.8 mM Ca^{2+}, 142 mM Na^+, 1.5 mM HPO_4^{3-}, 147.8 mM Cl^-, 5.0 mM K^+, 1.5 mM Mg^{2+}, 4.2 mM HCO_3^-, and 0.5 mM SO_4^{2-}. At different time points of mineralization (12 h, 1d, 2d, 4d, 14d), the chips were taken out, followed by washed with de-ionized water and dried for further characterizations.

2.6. X-ray diffraction

X-Ray Diffraction (XRD) was used to analyze the crystals (mineralization after 12 h, 1d, 2d) formed on different surfaces using a X-ray diffractometer (D/max-2500/PC, Rigaku, Japan) with the condition of Cu Kα1 radiation (λ = 0.1541 nm), 40 kV, 200 mA in a continuous θ-2θ scan model. The scanning range was 15° - 50° with a scanning speed of 4°/min and a step interval of 0.04°.

2.7. Scanning electron microscope (SEM)

The morphological features of the crystals (mineralization after 12 h, 1 d, 2 d, 4 d, 14 d) deposited on the surfaces were observed by SEM (JSM-7001F, JEOL, Japan). All the mineralized samples were dried and sputter-coated with 10 nm Pt layer and observed under an accelerating voltage of 20 kV.

2.8. Fourier transform infrared spectroscopy analysis

The crystals after mineralization of 14 days were examined by Fourier transform infrared spectroscopy (FTIR) (Spectrum GX, PerkinElmer, USA) at a resolution of 4 cm^{-1} and the range of wave length was from 4000 cm^{-1}–400 cm^{-1} to analyze the types of chemical bonds within the phosphate crystals. And the peaks from 1200 cm^{-1}–900 cm^{-1} were analyzed via the peak fitting function of Origin Pro 9, following a Gauss model.

3. Results

3.1. The hydrophilicity of the SAMs surfaces

The peptides underwent self-assembly on the Au substrates, which formed a peptide monolayer and changed the surface hydrophilicity obviously. Therefore, the water contact angles of different SAMs were examined to prove the successful self-assembly of the peptides, as presented in Table 1. The values of SAM-COOH, SAM-OH, and the pure Au substrate were in good agreement with the values shown in previous studies [32]. Among all the SAMs, SAM-OH revealed the best hydrophilicity and the values of peptide SAMs were mainly distributed between SAM-OH to SAM-COOH. These values showed that the peptide-treated samples had more hydrophilic surfaces than pure Au as expected, demonstrating that modified surfaces were successfully prepared via self-assembly of peptide monolayer onto Au (111) substrate. The contact angle reflected the differences in surface energy of different samples. Though DSS6 (DSS6G) and DSS9 (DSS9G) have the same terminal groups exposed outwards from the surface, the differences in the chain length and the side-chain functional groups also influenced the surface energy that contributed to the contact angle discrepancy in four peptide SAMs. For example, DSS6 (9) had smaller contact angle than DSS6 (9) G because the former had an additional –OH at the terminal and the latter just had a –COOH.

3.2. XPS analysis of the SAMs surface

The bonding of the peptides on Au substrates via interaction between gold and sulfur could be confirmed by using XPS analysis. Each peptide molecule contains one S atom, therefore, the densities of the assembled peptides may be estimated according to the area ratio between the S and Au atoms, which can be quantified by XPS analyses.

Table 1
Water contact angle (°) measured on the prepared SAMs.

DSS6	DSS6G	DSS9	DSS9G	COOH	OH	Au
18.0 ± 0.5	21.4 ± 1.0	14.5 ± 1.0	29.5 ± 1.0	29.4 ± 1.0	13.5 ± 0.5	55.0 ± 0.5

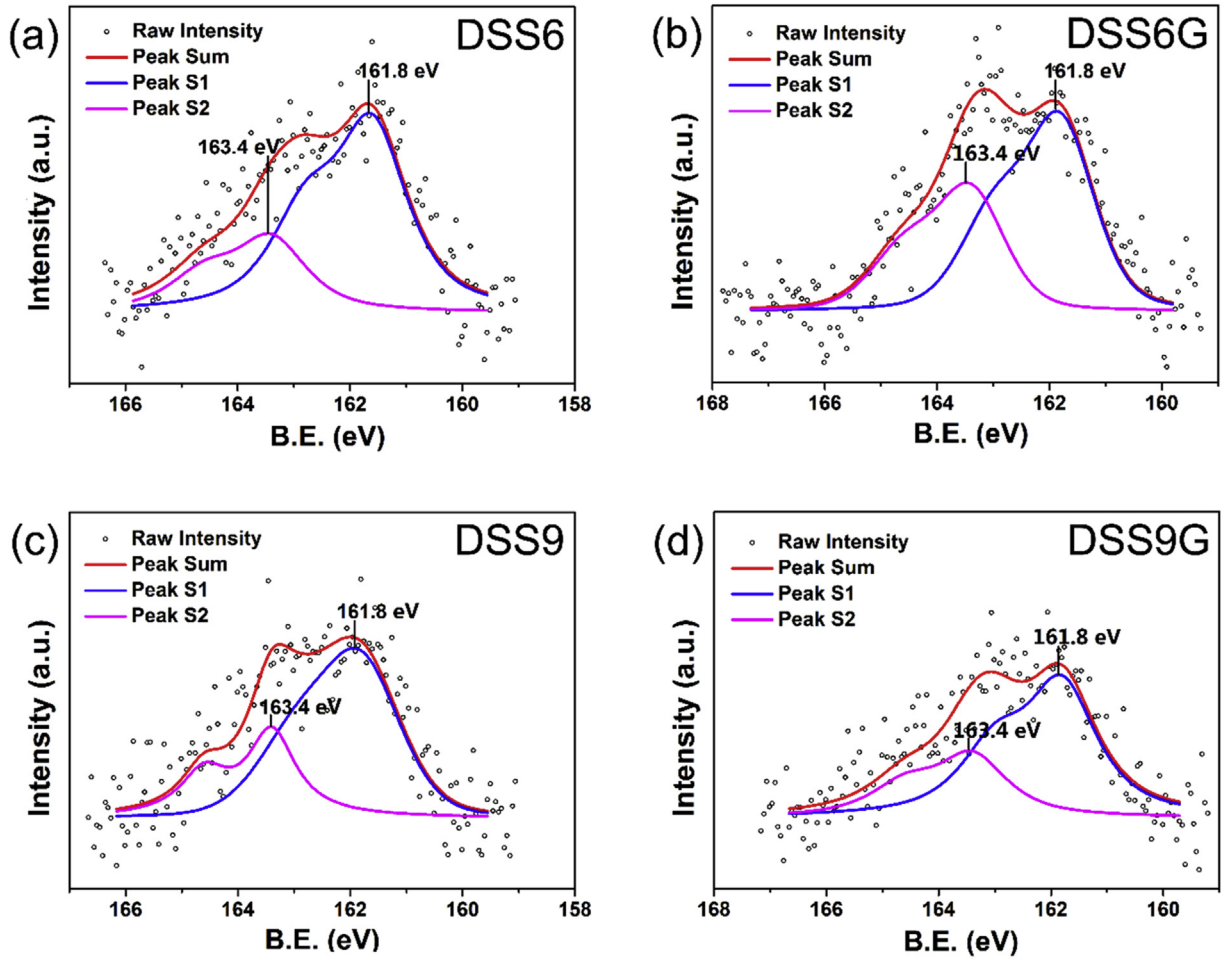

Fig. 2. XPS spectrum of sulfur 2p of SAM-DSS9, SAM-DSS6, SAM-DSS9G, SAM -DSS6G.

Table 2
Ratio of XPS peak integral area between S and Au atom (S/Au value) of different SAMs.

DSS6	DSS6G	DSS9	DSS9G	COOH	OH
0.056 ± 0.004	0.057 ± 0.003	0.069 ± 0.005	0.072 ± 0.006	0.189 ± 0.003	0.172 ± 0.004

The raw data of XPS were fitted as lines to show the chemical states of the S atom in different types of peptide monolayer, and the typical spectra for peptide SAMs were shown in Fig. 2. The spectral region of S 2p electron orbit showed two peaks (S1 and S2), both of which were complex peaks assigned to the $S_{2p3/2}$ and $S_{2p1/2}$ spin-orbit split levels. Deconvolution of the sulfur 2p emission line shape revealed the characteristic intensity ratio of 2:1 and the peak separation of 1.2 eV. In the spectra, S1 and S2 peaks indicated two totally different chemical states of the S atoms in peptides. The $S_{2p3/2}$ peak at 161.8 eV (S1) suggested the presence of an Au–S bond from the combination of thiol group and the Au (111) surface, indicating the existence of chemical reactions. Thus the chemisorption of the peptides was confirmed. Meanwhile, the S2 peak at 163.4 eV corresponded to the physisorption of peptides on the Au surface where no bond formation was happened. It is known to all that most of the photoelectron signals of XPS come from the surface region, thus the surface density of molecular distribution can be estimated by XPS results according to the detected ratio of peaks integral area between S and Au atoms (Table 2). All the samples were tested in same conditions where the penetration depth of X-ray used in XPS was supposed to be the same for all these SAM surfaces. Thus, we ignored X-ray reduction caused by differences in the type of peptide molecules. In other words, the ratio of different groups can be directly compared. The SAM-COOH has been proved to be a classical adsorption model, the grafting density of which is 4.6×10^{14} cm^{-2}. Thus, the grafting density of peptide SAMs could be estimated via S/Au ratio. The formula was as follows:

$$\frac{\text{density of peptide}}{4.6\times10^{14}\text{cm}^{-2}} = \frac{{}^{S}/_{Au}\text{ratio of peptide}}{{}^{S}/_{Au}\text{ratio of SAM}-\text{COOH}} \quad (1)$$

The results were revealed in Table 3, together with the size of peptide molecule models calculated via Chem3D software. Based on these sizes of peptide molecules, the theoretical grafting densities of peptide SAMs were listed in Table 3, including two situations: the

Table 3
Size of peptide molecule models and the grafting density of SAMs.

SAMs	DSS6	DSS6G	DSS9	DSS9G	COOH	OH
Diameter (Å)	7.9	7.8	7.9	7.9	/	/
Length (Å)	25	28.7	35.8	39.5	/	/
Density of standing up (cm^{-2})	1.76	1.8	1.76	1.76	/	/
Density of lying down (cm^{-2})	0.5	0.44	0.35	0.32	/	/
Density of estimating (*10^{14}cm^{-2})	1.36	1.39	1.68	1.75	4.6	4.2

Table 4
Zeta potential (mV) measured on the prepared SAMs.

COOH	OH	DSS6G	DSS6	DSS9G	DSS9	Au
−28.3 ± 4.8	−19.8 ± 1.0	−35.7 ± 3.0	−36.9 ± 4.1	−52.7 ± 1.5	−54.2 ± 2.5	−3.1 ± 2.3

peptide molecule 'standing up' as well as 'lying down'. And by comparing the values of theoretical densities and estimated densities, we found that the densities estimated from experimental data were closer to the 'standing up' density for all peptide SAM groups. Especially for SAM-DSS9 and SAM-DSS9G, the estimated values were almost same to the theoretical ones. These results suggested that most of the peptide molecules had good self-assembly on the Au substrates and preferred to be nearly perpendicular to the surfaces.

3.3. Zeta potential of the SAMs surface

The different surface energy and ionic charges of the SAMs obviously corresponded to the surface zeta potentials. The results of zeta potential of all samples were listed in Table 4. The zeta potentials of peptide SAMs were generally much lower than SAM-COOH, although their terminal functional group were same. For SAM-COOH, the theoretical density of –COOH was higher than peptide SAMs due to a higher molecular density. The much lower zeta potential values could be attributed to the residue group of –COOH in aspartic acid. In addition, an extra DSS repeat could reduce the zeta potential values judging from the results of DSS6 (G) and DSS9 (G). This indicated that the side chain groups in peptide SAMs also affected the surface potential, although they were not directly exposed on the surface.

3.4. XRD pattern analysis of the mineralized crystals

The composition and crystal type of the mineralized products were analyzed via X-ray diffraction pattern. The XRD pattern (Fig. 3) showed obvious variation of peak position and intensity during the mineralization process in the experimental groups, revealing the nucleation and growth of calcium phosphate minerals. First of all, as the immersion time increased, the peak at 31.7° (31.67° ~31.74°) that was assigned to HAp (211) crystal face firstly appeared successively on different SAMs. After 12 h of immersion, the HAp (211) peak were detected only on SAM-DSS9/DSS9G sample groups, while no characteristic diffraction peaks of HAp were observed on the other samples. After 1d of immersion, HAp (211) peak started to appeared on SAM-DSS6/DSS6G samples. After 2d of immersion, a small HAp (211) peak was finally recognized on the XRD pattern of SAM-COOH, whereas there's no any diffraction peak on SAM-OH yet. The results indicated that nucleation rate of HAp minerals was highly regulated by the SAMs templates. The HAp nucleation was remarkably promoted by the SAM-DSS9/DSS9G, followed by the SAM-DSS6/DSS6G and the SAM-COOH. And the SAM-OH had the weakest capacity to promote HAp nucleation. Secondly, it's noted that the peak intensities that implied the amount of HAp crystals increased dramatically over time on different SAMs surfaces. Besides, the HAp (211) peak on SAM-DSS9/DSS9G spectrum became sharper and sharper with the increase of immersion time, judging from the results of 12 h and 1d of results, which indicated the increased crystallinity and highest rate of crystal growth. While there was no obvious enhancement from day 1 to day 2 on SAM-DSS6/DSS6G. More than that, the characteristic peaks of HAp (200) at 21.6° (21.57° ~21.63°) also emerged at 2 days of immersion on SAM-$(DSS)_n$ and SAM-COOH samples. However, XRD pattern of SAM-OH only showed the peak of HAp (200). No sign of HAp (211) peak appeared within four days. In addition, no peaks founded on the control group,

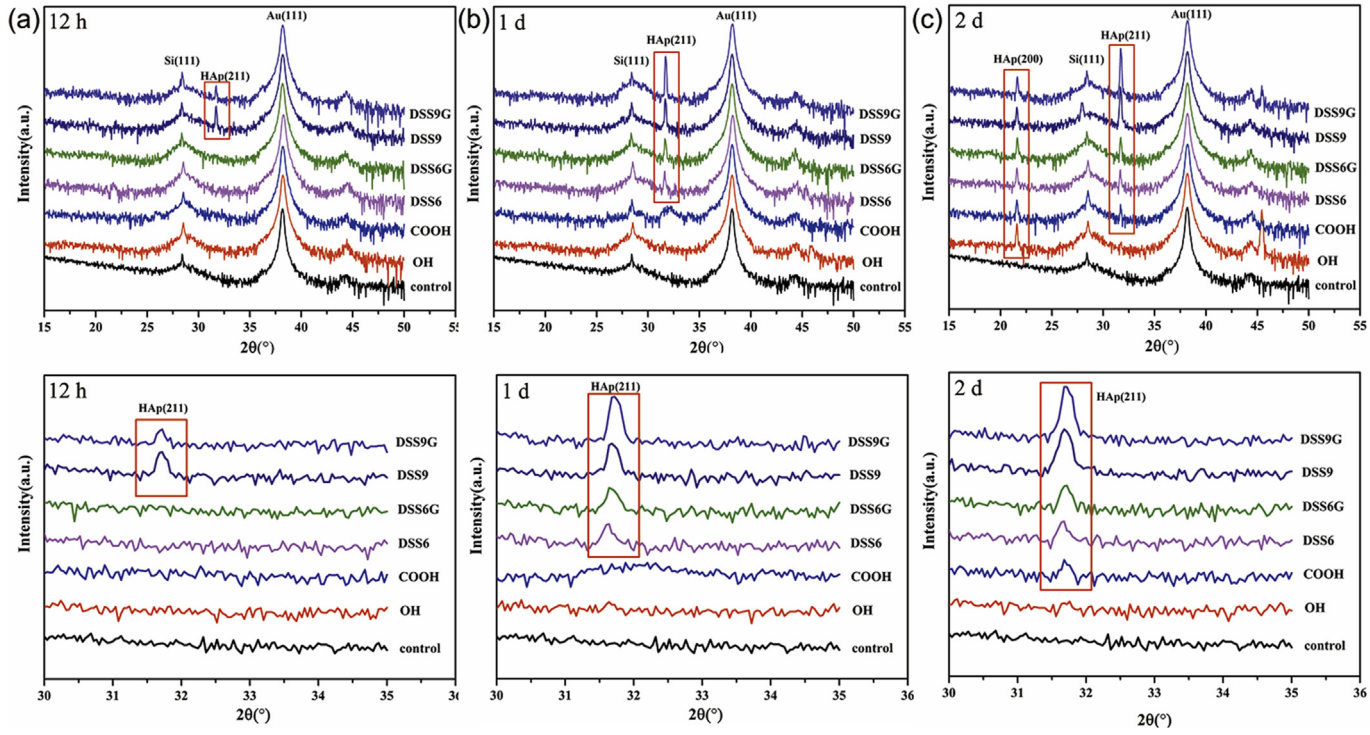

Fig. 3. XRD pattern of SAM-DSS9, SAM-DSS6, SAM-DSS9G, SAM-DSS6G, SAM-COOH, and SAM-OH surface after (a)12 h, (b)1d and (c)2d of immersion into 1.5 SBF. Four positions of peak were shown: Si(111), HAp(211), HAp(200) and Au(111) and the HAp(211) peaks were marked by red rectangle. (For interpretation of the references to colour in this figure legend, the reader is referred to the Web version of this article.)

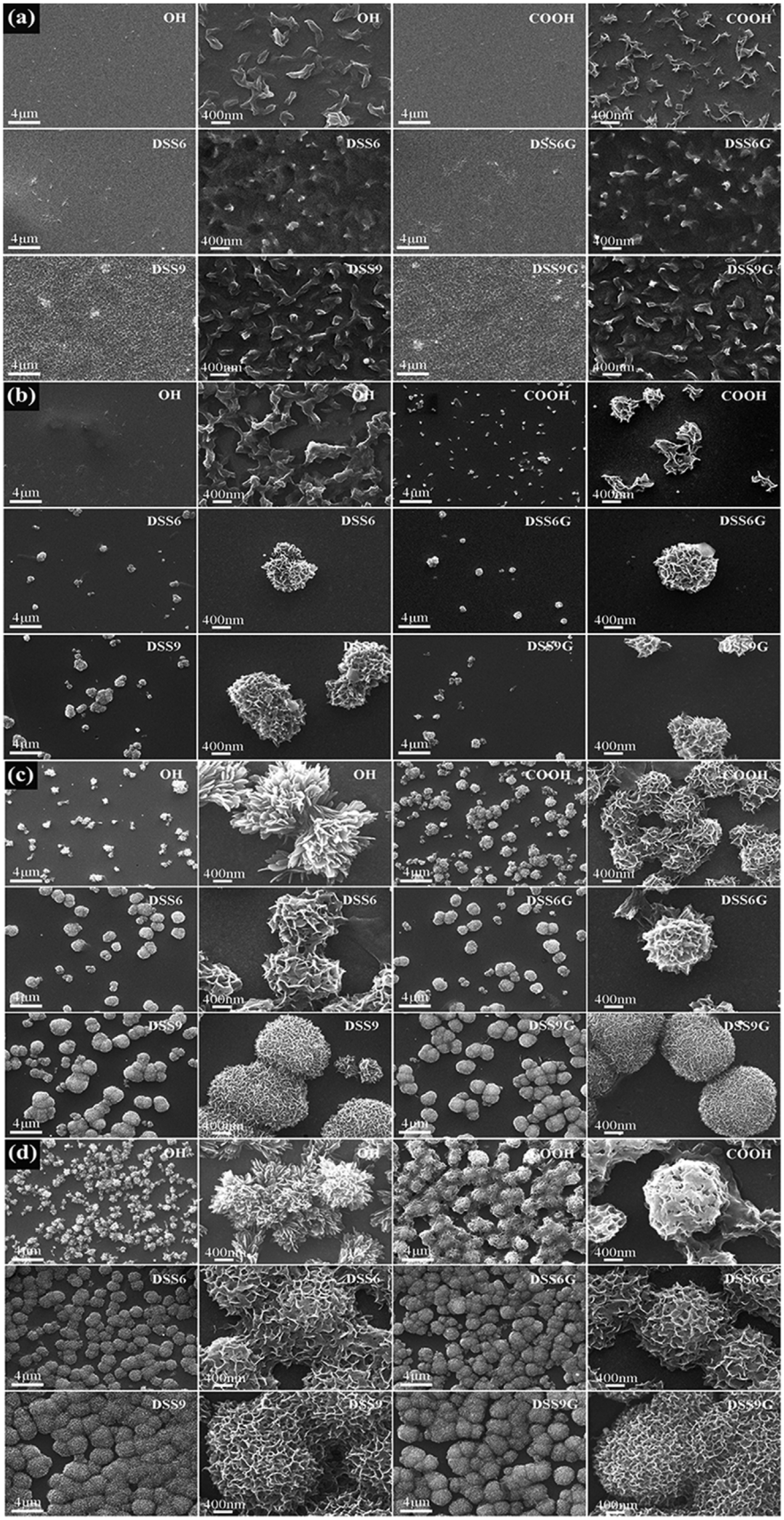

Fig. 4. SEM image of SAM-DSS9, SAM-DSS6, SAM-DSS9G, SAM-DSS6G, SAM-COOH, and SAM-OH surface after (a)12 h, (b)1d, (c)2d, and (d)4d of immersion into 1.5 SBF.

indicating that Au substrate could not induce HAp mineralization.

3.5. SEM morphology of the mineralized crystals

The SEM images clearly exhibited the typical morphologies of minerals deposited on the SAMs surfaces at the different time points, as shown in Fig. 4. In according with the XRD results, at 12 h after immersion (Fig. 4a), irregular tiny particles that should be amorphous Ca–P nuclei uniformly deposited onto the SAMs surfaces. It could be clearly seen that the densities and sizes of the nucleated particles on SAM-DSS9/DSS9G were much larger than any other SAM groups with about 400 nm in length, as shown in the magnified images. After 1 day of immersion, minerals on SAM-DSS9/DSS9G grew bigger and bigger with 1.5 μm in diameter (Fig. 4b), while on SAM-DSS6/DSS6G, they were about 800 nm large. The precipitated minerals on both of DSS9/DSS9G and DSS6/DSS6G groups showed a plate-like microstructure, indicating the phase transformation from the amorphous to crystalline calcium phosphate, which was consistent with the XRD results. What's more, the particles on SAM-COOH also showed a typical crystalline morphology but with much smaller size. However, the tiny particles deposited on SAM-OH almost had no changes in appearance. After 2-day immersion (Fig. 4c), the plate-like crystals on SAM-DSS9/DSS9G grew into bigger round spheres with almost 3 μm in diameter, which distributed uniformly. The morphology of mineralized spheres on SAM-DSS6/DSS6G was similar to that on SAM-DSS9/DSS9G, although the density and size were much smaller. At this time, the nucleation density on the SAM-COOH surface was similar to SAM-$(DSS)_n$, but the size was only about 1 μm. Furthermore, crystal flakes of HAp on SAM-DSS9/DSS9G showed obviously densification, while crystal flakes on other samples were relatively loose-packed. The differences in mineral sphere densities and crystal flakes implied that SAM-DSS9/DSS9G accelerated the crystal nucleation and growth most efficiently, followed by SAM-DSS6/DSS6G and SAM-COOH. While SAM-OH showed poor ability to mediate HAp formation. After 4 days' immersion (Fig. 4d), the spherical crystals on SAM-$(DSS)_n$ continued to grow bigger and bigger and the densities notablely increased, thus the spheres almost touched each other and formed continuous coatings. As for the SAM-COOH/OH, the density also showed significant increased, and a layer of minerals consisting of uniform spherical crystals with about 2 μm in diameter was formed on SAM-COOH. However, the size of minerals on SAM-OH was still very small.

After 14-day mineralization in SBF, cross section morphologies were observed by SEM. As shown in Fig. 5, the thickness of the semi-spherical crystals on SAM-DSS9/DSS9G were 4–5 μm. While for SAM-DSS6/DSS6G, the mineral layer was no more than 3 μm in thickness and for SAM-COOH the value was under 2 μm. In the case of SAM-OH, the mineral layer was only about 0.5 μm and the shapes of crystal were utterly different. Only a few minerals were scattered on the surface, not forming an intact mineral layer.

3.6. FTIR analysis

The obtained FTIR spectra and the corresponding curve fit results were shown in Fig. 6. FTIR spectroscopic analysis of the HAp crystals, formed after 14 days of mineralization, showed three main absorption region of hydroxide, carbonate and phosphate. And there were notable differences among different substrates in the $\nu 3$ phosphate absorption region (900–1200 cm^{-1}) that could give information on the HAp crystallinity. This broad contour is constituted of several underlying peaks (960 cm^{-1}, 985 cm^{-1}, 1020 cm^{-1}, 1030 cm^{-1}, 1055 cm^{-1}, 1075 cm^{-1}, 1096 cm^{-1}, 1116 cm^{-1}, and 1145 cm^{-1}) presenting different specific phosphate environments, in which two main peaks at 1020 and 1030 cm^{-1} should be noticed. Peaks at 1020 cm^{-1} were attributable to nonstoichiometry and/or the presence of acid phosphate-containing species and peaks at 1030 cm^{-1} can be assigned to molecular vibrations of the phosphate (PO_4^{3-}) moiety in an apatitic/stoichiometric environment of HAp. Previous studies showed that at early stages of mineralization in all samples of HAp mineral, the 1020 cm^{-1} band dominates. However, during maturation and aging, the 1030 cm^{-1} band gradually becomes the most intense band, and, in fully mineralized enamel, the 1020 cm^{-1} band is barely observable [2,3,10,13]

Subsequently, we calculated the area ratio of integral area of 1020 cm^{-1} and 1030 cm^{-1} peaks (Table 5) and the area ratio of 1030/1020 (Table 6) that previously has been used to analyze the degree of crystallinity and maturity of the HAp minerals. The Mineral particles formed on SAM-DSS6G (sum of 1300 cm^{-1} and 1200 cm^{-1} area: 67.27%) and SAM-DSS9G (sum of 1300 cm^{-1} and 1200 cm^{-1} area: 62.70%) surfaces exhibited better degree of crystallinity than that on SAM-COOH (sum of 1300 cm^{-1} and 1200 cm^{-1} area: 43.22%). Meanwhile, the HAp on SAM-DSS9G (1030/1020: 4.6074) and SAM-DSS6G (1030/1020: 1.5931) showed obviously superiority of crystal maturity compared with SAM-COOH (1030/1020: 0.8973).

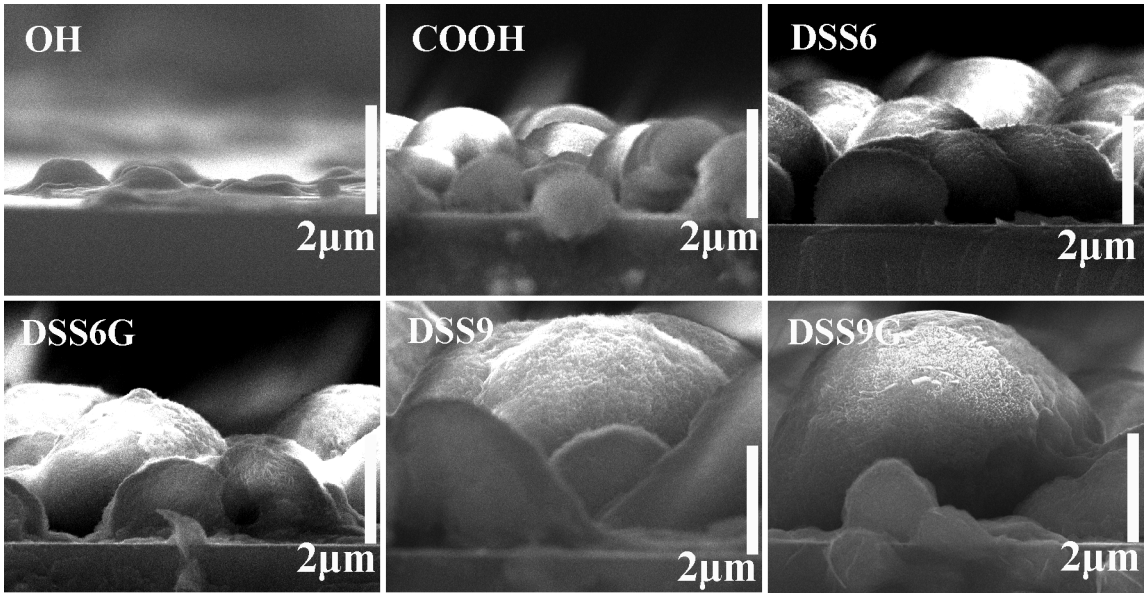

Fig. 5. SEM images of SAM-$(DSS)_n$/COOH/OH cross section after 14 d of biomineralization.

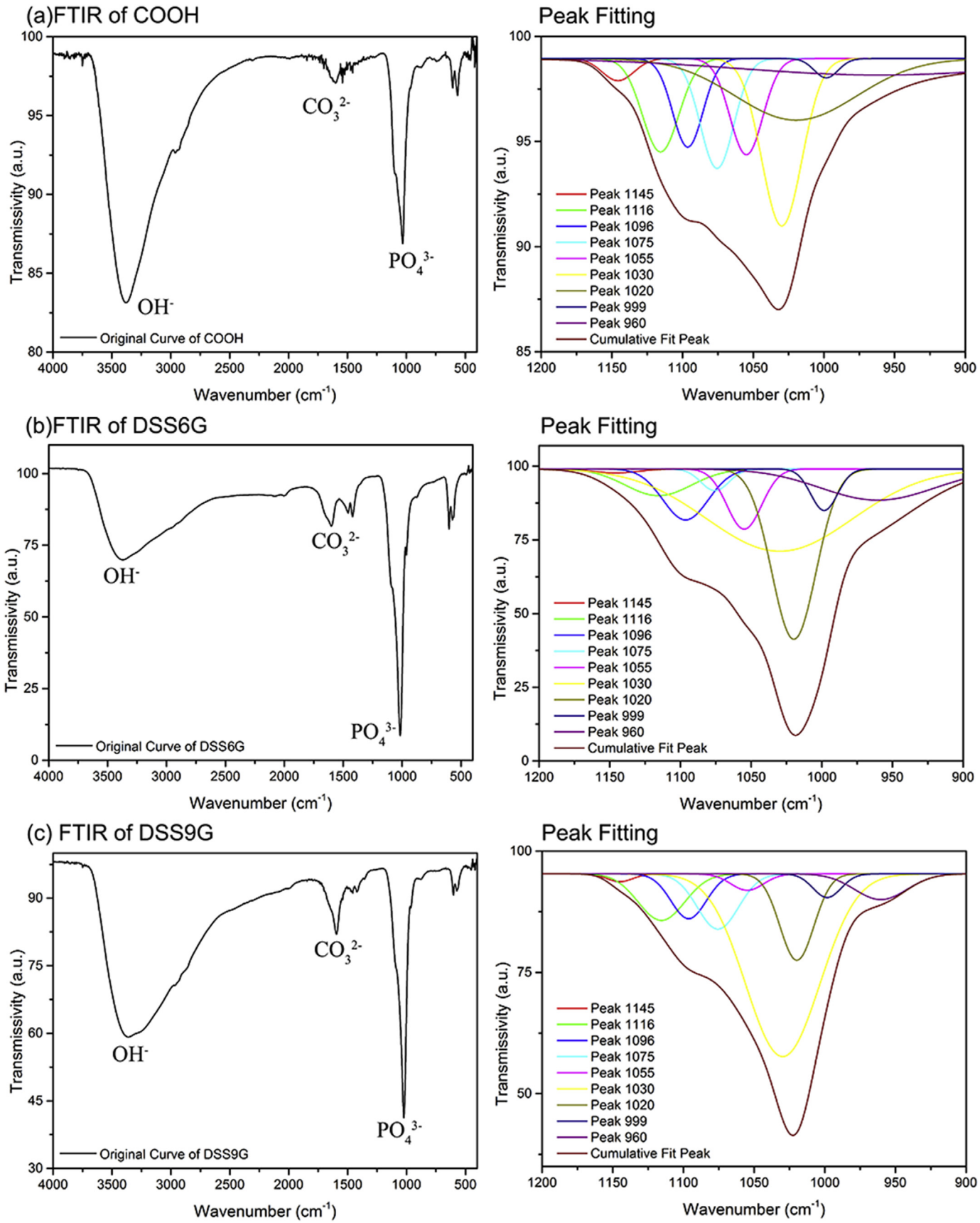

Fig. 6. FTIR spectra and corresponding curve fit of (a) SAM-COOH, (b) SAM-DSS6G, (c) SAM-DSS9G.

Table 5
Area ratio of integral area of 1030 cm^{-1} and 1020 cm^{-1} peaks of FTIR.

SAMs	% Area (1030 cm^{-1})	% Area (1020 cm^{-1})
-COOH	20.44	22.78
DSS6G	38.52	24.18
DSS9G	53.63	11.64

*% Area indicates the percentage of the peak area of a certain peak accounting for the total area.

Table 6
Integral Area ratio of 1030 cm^{-1}/1020 cm^{-1} peaks of FTIR.

-COOH	DSS6G	DSS9G
0.8973	1.5931	4.6074

4. Discussion

In order to investigate the effect of the repeated tripeptide DSS widely presented in non-collagenous glycoproteins on HAp mineralization, the SAM-DSS_n were successfully fabricated in this study, which provided a simply and quantitative mineralization model to investigate the influences of the DSS sequence as the analog of non-collagenous proteins on calcium phosphate biomineralization in a SBF environment.

The DSS repeated peptides terminated with cysteine could form good peptide self-assembled monolayers on Au substrates, which provided highly anionic surfaces enriched in carboxyl functional groups. According to the classic biomineralization principle——'interfacial molecular recognition' mechanism, it is suggested that the anionic groups such as –COOH initially form strong electrostatic bonds with Ca^{2+} ions and then these calcium ions accumulated at specific sites on the surface attracted sufficient numbers of phosphate anions so that nucleation of calcium phosphate minerals occurred. Besides, the hydroxyl groups that exist mostly in polysaccharides and proteins enriched in serine and threonine amino acids are known to be important in controlling mineral deposition through polar interactions between –OH and Ca^{2+} ions. In this study, we found the consistent results that all the SAM-$(DSS)_n$ as well as SAM-COOH and SAM-OH control groups showed the positive effects on mediating HAp mineralization, while no any mineral deposition was observed on pure Au substrate. In addition, the SAMs with carboxyl surfaces showed much higher capacities to mediate HAp nucleation and growth than SAM-OH, indicating the strong electrostatic bond between –COOH and Ca^{2+} ions was a very important factor in organic matrix-mediated biomineralization. Nevertheless, it's worth noting that all the peptide SAMs (SAM-$(DSS)_n$) induced Ca–P nucleation much earlier than alkanethiol SAM-COOH, and the calcium phosphate minerals deposited on SAM-$(DSS)_n$ grew much faster, judging from both the XRD and SEM results, although they had the same terminal carboxyl groups on the surfaces. According to XPS examination, the area ratio of S/Au on SAM-COOH was much higher than those on peptide SAMs, which implied the densities of –COOH on SAM-COOH should be much higher than any other peptide SAMs. Therefore, it's reasonable to assume that the amount of carboxyl group presented on the surface of the template is not a direct key factor related to the biomineralization process, though the carboxyl group provides a strong molecular recognition at the organic-inorganic interfaces. We estimated that those polar and acidic amino acids in the repeated DSS peptides also had great contributions on biomineralization, although they were not fully exposed on the surface of the SAMs. The results of zeta potential of the SAMs surfaces confirmed our hypothesis. The SAM-$(DSS)_n$ had more negative zeta potentials than the SAM-COOH surface, meaning relative higher surface energy and the electronegativity of which were quite considerable for Ca^{2+} absorption in SBF to reduce the surface potential as possible. Therefore, those acidic-rich domains in non-collagenous glycoproteins not only provide strong affinity with Ca^{2+} ions through direct electrostatic bonds, but more importantly influence surface electrostatic potentials of the assembled organic template with reduced activation energy for nucleation.

Consequentially, the length of the acidic-rich domains should contribute to the biomineralization process. In this study, the SAM-DSS9/DSS9G exhibited higher capacity on inducing nucleation and mineral growth than the SAM-DSS6/DSS6G. As early as 12 h after immersion into 1.5 SBF, nano-size particles of Ca–P had formed on SAM-DSS9/DSS9G and finally grew into hemisphere micro-crystals with 5 μm in diameter after 14 days of mineralization. For SAM-DSS6/DSS6G, the nucleation occurred later than SAM-DSS9/DSS9G according to the late appearance of HAp (211) peak in XRD pattern. What is more, the quantity and size of Ca–P nuclei as well as the size of mineral particles on SAM-DSS6/DSS6G were always smaller than those on SAM-DSS9/DSS9G at each time point during the whole mineralization process. We believed that the differences should attribute to one more DSS repeat of DSS9/DSS9G. Considering that one molecule of DSS9/DSS9G peptide contained not only one carboxyl at terminal, but other three residue group of carboxyl as side chains, the DSS9/DSS9G template would be much more negatively charged than other surfaces, and thus possessed the highest electrostatic absorbability and complicated hydrogen bond systems. The relative complicated structure of peptides could increase the surface electronegativity via the addition of DSS sequence. The electrostatic potential distribution and dipole moment results of each single peptide molecule were computation via Gaussian (Fig. 7, Functional: M062X; Basis set: 6-31 + G**). And the dipole moment values revealed that as the peptide got longer, the μ increased. It meant that DSS9/DSS9G was with higher polarity than DSS6/DSS6G leading to higher attraction of Ca^{2+} when the molecules forming SAMs. Thus, SAM-DSS9/DSS9G owned a high rate of nucleation of HAp and induced

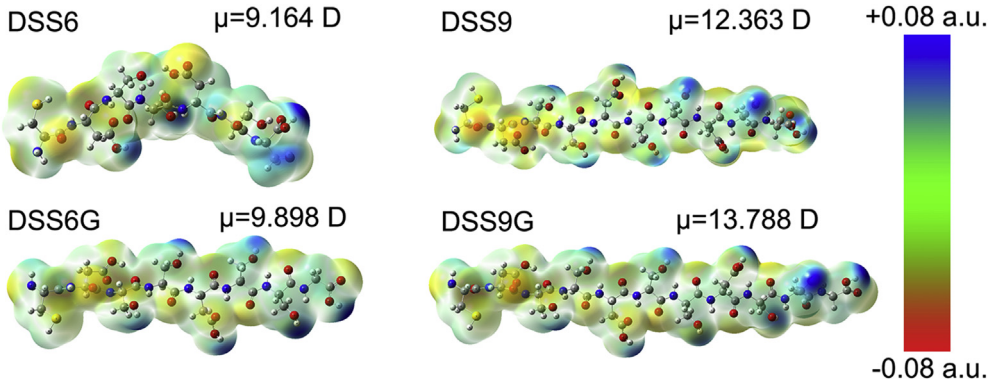

Fig. 7. Electrostatic potential distribution and dipole moment results of four peptide molecules.

crystalline deposition with rapid growing speed and larger size of crystal spheres. Beyond that, SAMs provided uniformly organized molecules patterns with periodically aligned –COOH groups, which is beneficial to the accumulation of Ca^{2+} and crystalline nucleation.

Moreover, it's noted that the differences during the mineralization process mainly occurred between the peptide SAMs with different length of DSS. The effects of extra terminal amino acid glycine were not so obvious. On the SAM-DSS6 and SAM-DSS9, the terminal amino acid serine had one –COOH and one –OH side group, while the terminal amino acid glycine on SAM-DSS6G and SAM-DSS9G only had one –COOH, which indicated the hydroxyl groups of serine exposed on the surface of SAM-DSS6 and SAM-DSS9 didn't contribute too much for HAp mineralization.

Previous studies have shown that both ion adsorption and cluster adsorption are possible mechanisms of mineralization [4,7,21]. We believe that both of the mechanisms existed in our study. According to particle-based mechanism, pre-nucleation clusters were formed firstly around the template and then aggregated to small amorphous nanoparticles above the substrate with negative charge. According to our results, it is conceivable that the particle-based mechanism also existed in the nucleation and growth process of HAp, because we could observe small amorphous particles started to take shape onto the template at the first 12 h and no characteristic peaks were found in XRD results except the DSS9/DSS9G group. And the use of the 1.5 SBF increased the possibility because the ions of both Ca^{2+} and PO_4^{3+} were supersaturated in the environment. If the substrates was pre-calcified by saturated solution calcium salt, Ca^{2+} ion adsorption and nucleation by molecular recognition would be the main mechanism. However, in this manuscript, we were focusing only on the function of the $(DSS)_n$ peptide while leaving the mechanism selectivity for a future work.

Some previous studies on SAMs-based bio-mineralization were limited to the range of alkanethiols with different functional group [30–32]. These models could be considered as ideal two-dimensional models, in which the terminal groups were the most important factor. It was not a suitable model for further research on calcium phosphate biomineralization due to the complicated structure of collagen template as well as induced non-collagenous proteins. In our previous study, we mixed non-collagenous peptide with collagen to observe the calcium phosphate biomineralization on organic template, however it was difficult to distinguish the precise effects of peptide without a regular and quantitative model [40]. But this time, we got some further understanding on how the repeat DSS sequences changed the surface potential to accelerate nucleation and HAp crystal growth. With above understanding obtained from the experimental phenomena of HAp nucleation induced by SAM-$(DSS)_n$, we can considered that, the efficiency of crystal nucleation and growth were mainly adjusted by surface energy, which were influenced by potential and polarity of the organic matrix. The structure of designed DSS peptide would change the whole potential of substrate surface by change the amount of side chain. And simply repeated DSS sequences had the ability of inducing the formation of HAp in a SAM model.

It will be a constructive reference when a modified surface is designed to realize high-efficient mineralization, such as in the therapy of saprodontia in clinic. And the study is of great significance to deeply understand the formation mechanism of bone and dental tissue, as well as the design and preparation of functional biomimetic materials.

5. Conclusion

In this study, the biomimetic peptides DSS9/DSS9G/DSS6/DSS6G were designed and successfully self-assembled onto Au (111) substrate, forming uniform peptide SAMs for calcium phosphate mineralization in SBF environment, in comparison with other two kinds of self-assembled alkanethiols surfaces. The SAM-DSS9/DSS9G showed the highest nucleation efficiency, followed by SAM-DSS6/DSS6G, SAM-COOH, and SAM-OH. The quantity and size of Ca–P nuclei as well as the size of mineral particles on SAM-DSS9/DSS9G were always larger than any other group at each time point during the whole mineralization process. The SAM-$(DSS)_n$ had more negative zeta potentials than SAM-COOH surface, indicating that DSS repeats contributed to the biomineralization, which not only provided strong affinity with Ca^{2+} ions through direct electrostatic bonds, but more importantly influence surface electrostatic potentials of the assembled organic template for nucleation.

Credit author statement

We declare that this manuscript has not been published previously, and that it is not under consideration for publication elsewhere. All the authors have confirmed the submission of this manuscript.

CRediT authorship contribution statement

Shuo Wang: Investigation, Data curation, Formal analysis, Writing - original draft, Writing - review & editing. **Yongdong Yang:** Project administration, Resources, Formal analysis, Validation. **Ronghan Wang:** Methodology, Data curation, Validation, Visualization. **Xiangdong Kong:** Software, Resources. **Xiumei Wang:** Conceptualization, Funding acquisition, Supervision, Writing - review & editing.

Declaration of competing interest

We declare that we have no conflict of interest.

Acknowledgement

This work was supported by the National Natural Science Foundation of China (No. 31771056).

References

[1] J. Venkatesan, S.K. Kim, Nano-hydroxyapatite composite biomaterials for bone tissue engineering–a review, J. Biomed. Nanotechnol. 10 (2014) 3124–3140.
[2] A. Haider, S. Haider, S.S. Han, I.-K. Kang, Recent advances in the synthesis, functionalization and biomedical applications of hydroxyapatite: a review, RSC Adv. 7 (2017) 7442–7458.
[3] A. Szczes, L. Holysz, E. Chibowski, Synthesis of hydroxyapatite for biomedical applications, Adv. Colloid Interface Sci. 249 (2017) 321–330.
[4] L.B. Gower, Biomimetic model systems for investigating the amorphous precursor pathway and its role in biomineralization, Chem. Rev. 108 (2008) 4551–4627.
[5] P. Zhu, Y. Masuda, K. Koumoto, The effect of surface charge on hydroxyapatite nucleation, Biomaterials 25 (2004) 3915–3921.
[6] S. Gajjeraman, K. Narayanan, J. Hao, C. Qin, A. George, Matrix macromolecules in hard tissues control the nucleation and hierarchical assembly of hydroxyapatite, J. Biol. Chem. 282 (2007) 1193–1204.
[7] S. Bodhak, S. Bose, A. Bandyopadhyay, Role of surface charge and wettability on early stage mineralization and bone cell-materials interactions of polarized hydroxyapatite, Acta Biomater. 5 (2009) 2178–2188.
[8] A. Doostmohammadi, A. Monshi, R. Salehi, M.H. Fathi, Z. Golniya, A.U. Daniels, Bioactive glass nanoparticles with negative zeta potential, Ceram. Int. 37 (2011) 2311–2316.
[9] Z. Fang, Y. Zhao, H. Wang, J. Wang, S. Zhu, Y. Jia, J.-H. Cho, S. Guan, Influence of surface charge density on ligand-metal bonding: a DFT study of NH3 and HCOOH on Mg (0 0 0 1) surface, Appl. Surf. Sci. 470 (2019) 893–898.
[10] F. Nudelman, K. Pieterse, A. George, P.H. Bomans, H. Friedrich, L.J. Brylka, P.A. Hilbers, G. de With, N.A. Sommerdijk, The role of collagen in bone apatite formation in the presence of hydroxyapatite nucleation inhibitors, Nat. Mater. 9 (2010) 1004–1009.
[11] A. Mata, Y. Geng, K.J. Henrikson, C. Aparicio, S.R. Stock, R.L. Satcher, S.I. Stupp, Bone regeneration mediated by biomimetic mineralization of a nanofiber matrix, Biomaterials 31 (2010) 6004–6012.
[12] L.C. Palmer, C.J. Newcomb, S.R. Kaltz, E.D. Spoerke, S.I. Stupp, Biomimetic systems for hydroxyapatite mineralization inspired by bone and enamel, Chem. Rev. 108 (2008) 4754–4783.
[13] J. Hao, A. Ramachandran, A. George, Temporal and spatial localization of the dentin matrix proteins during dentin biomineralization, J. Histochem. Cytochem. 57 (2009) 227–237.
[14] K. Alvares, The role of acidic phosphoproteins in biomineralization, Connect. Tissue Res. 55 (2014) 34–40.

[15] M. Prasad, W.T. Butler, C. Qin, Dentin sialophosphoprotein in biomineralization, Connect. Tissue Res. 51 (2010) 404–417.
[16] J. Ryu, S.H. Ku, H. Lee, C.B. Park, Mussel-Inspired polydopamine coating as a universal route to hydroxyapatite crystallization, Adv. Funct. Mater. 20 (2010) 2132–2139.
[17] X. Chu, W. Jiang, Z. Zhang, Y. Yan, H. Pan, X. Xu, R. Tang, Unique roles of acidic amino acids in phase transformation of calcium phosphates, J. Phys. Chem. B 115 (2011) 1151–1157.
[18] A. George, A. Veis, Phosphorylated proteins and control over apatite nucleation, crystal growth, and inhibition, Chem. Rev. 108 (2008) 4670–4693.
[19] W.T. Butler, J.C. Brunn, C. Qin, M.D. McKee, Extracellular matrix proteins and the dynamics of dentin formation, Connect. Tissue Res. 43 (2002) 301–307.
[20] L. Wang, G.H. Nancollas, Calcium orthophosphates: crystallization and dissolution, Chem. Rev. 108 (2008) 4628–4669.
[21] K. Schilling, S.T. Brown, L.N. Lammers, Mineralogical, nanostructural, and Ca isotopic evidence for non-classical calcium phosphate mineralization at circum-neutral pH, Geochem. Cosmochim. Acta 241 (2018) 255–271.
[22] B.K. Culpepper, M.C. Phipps, P.P. Bonvallet, S.L. Bellis, Enhancement of peptide coupling to hydroxyapatite and implant osseointegration through collagen mimetic peptide modified with a polyglutamate domain, Biomaterials 31 (2010) 9586–9594.
[23] Z. Huang, C.J. Newcomb, P. Bringas Jr., S.I. Stupp, M.L. Snead, Biological synthesis of tooth enamel instructed by an artificial matrix, Biomaterials 31 (2010) 9202–9211.
[24] M. Tavafoghi, M. Cerruti, The role of amino acids in hydroxyapatite mineralization, J. R. Soc. Interface 13 (2016).
[25] H.Y. Chung, C.C. Li, C.C. Hsu, Characterization of the effects of 3DSS peptide on remineralized enamel in artificial saliva, J. Mech. Behav. Biomed. Mater. 6 (2012) 74–79.
[26] W. Zhang, X. Yu, Y. Li, Z. Su, K.D. Jandt, G. Wei, Protein-mimetic peptide nanofibers: motif design, self-assembly synthesis, and sequence-specific biomedical applications, Prog. Polym. Sci. 80 (2018) 94–124.
[27] B.J. Tarasevich, C.J. Howard, J.L. Larson, M.L. Snead, J.P. Simmer, M. Paine, W.J. Shaw, The nucleation and growth of calcium phosphate by amelogenin, J. Cryst. Growth 304 (2007) 407–415.
[28] D.K. Yarbrough, E. Hagerman, R. Eckert, J. He, H. Choi, N. Cao, K. Le, J. Hedger, F. Qi, M. Anderson, B. Rutherford, B. Wu, S. Tetradis, W. Shi, Specific binding and mineralization of calcified surfaces by small peptides, Calcif. Tissue Int. 86 (2010) 58–66.
[29] Y. Wang, B.H. Ding, S.Y. Gao, X.B. Chen, R.C. Zeng, L.Y. Cui, S.J. Li, S.Q. Li, Y.H. Zou, E.H. Han, S.K. Guan, Q.Y. Liu, In vitro corrosion of pure Mg in phosphate buffer solution-Influences of isoelectric point and molecular structure of amino acids, Mater. Sci. Eng. C Mater. Biol. Appl. 105 (2019) 110042.
[30] G.K. Toworfe, R.J. Composto, I.M. Shapiro, P. Ducheyne, Nucleation and growth of calcium phosphate on amine-, carboxyl- and hydroxyl-silane self-assembled monolayers, Biomaterials 27 (2006) 631–642.
[31] Z.-X. Liu, X.-M. Wang, Q. Wang, X.-C. Shen, H. Liang, F.-Z. Cui, Evolution of calcium phosphate crystallization on three functional group surfaces with the same surface density, CrystEngComm 14 (2012) 6695.
[32] H. Deng, X.-M. Wang, C. Du, X.-C. Shen, F.-Z. Cui, Combined effect of ion concentration and functional groups on surface chemistry modulated CaCO3 crystallization, CrystEngComm 14 (2012) 6647.
[33] S.C. Freitas, A. Correa-Uribe, M.C.L. Martins, A. Pelaez-Vargas, Self-assembled monolayers for dental implants, Int. J. Dent. 2018 (2018) 4395460.
[34] A. Janković, S. Eraković, M. Mitrić, I.Z. Matić, Z.D. Juranić, G.C.P. Tsui, C.-y. Tang, V. Mišković-Stanković, K.Y. Rhee, S.J. Park, Bioactive hydroxyapatite/graphene composite coating and its corrosion stability in simulated body fluid, J. Alloys Compd. 624 (2015) 148–157.
[35] D.F. Laird, M.R. Mucalo, Y. Yokogawa, Growth of calcium hydroxyapatite (Ca-HAp) on cholesterol and cholestanol crystals from a simulated body fluid: a possible insight into the pathological calcifications associated with atherosclerosis, J. Colloid Interface Sci. 295 (2006) 348–363.
[36] T. Kokubo, H. Takadama, How useful is SBF in predicting in vivo bone bioactivity? Biomaterials 27 (2006) 2907–2915.
[37] X. Yao, Y. Song, L. Jiang, Applications of bio-inspired special wettable surfaces, Adv. Mater. 23 (2011) 719–734.
[38] X. Li, J. Wei, K.E. Aifantis, Y. Fan, Q. Feng, F.Z. Cui, F. Watari, Current investigations into magnetic nanoparticles for biomedical applications, J. Biomed. Mater. Res. 104 (2016) 1285–1296.
[39] Z. Ke, F. Yubo, D. Nicholas, L. Xiaoming, Effect of microporosity on scaffolds for bone tissue engineering, Regen. Biomater. (2018) 5.
[40] Q. Wang, X.M. Wang, L.L. Tian, Z.J. Cheng, F.Z. Cui, In situ remineralizaiton of partially demineralized human dentine mediated by a biomimetic non-collagen peptide, Soft Matter 7 (2011) 9673.